

On the synthesis and design of a novel backdrivable high-stiffness capstan drive

Jordan M. Longval and Clément Gosselin

Département de génie mécanique

Université Laval

1065 Avenue de la Médecine

Québec, Qc G1V0A6

Canada

Jordan.Longval.1@ulaval.ca, Clement.Gosselin@gmc.ulaval.ca

This article introduces a novel backdrivable high-stiffness cable capstan drive architecture for robotics applications. The drive has a low transmission ratio and a higher stiffness than typical capstan drives. The higher transmission stiffness is obtained by the use of grooves on both the input and the output pulleys of the drive which increases the effective coefficient of friction between the pulleys and the cable. The groove on the input pulley forms a single helix while the grooves on the output pulley form a R-helix, where R is equal to the transmission ratio of the drive. This property enables several different multi-cable arrangements for the drive, which further increases the transmission stiffness. A kinematic model of the capstan drive is established and used to ensure the proper alignment of the input pulley groove and output pulley grooves as a function of the distance between the pulleys. A 3D printed prototype of the transmission is presented.

1 Introduction

Robotic manipulators typically use transmissions with large reduction ratios in order to reduce the size and mass of the actuators. Such transmissions (e.g. harmonic drives) are not backdrivable, which is a limitation in some applications. For example, in Collaborative Robots (CR), it is desired to provide physical Human-Robot Interaction (pHRI), i.e., to allow users to manipulate the robot links directly.

Because their transmissions are not backdrivable, most CR used nowadays require force sensors to enable task teaching through pHRI. The force sensors are either placed near the CR's end effector [1] [2] [3] or inside each joint of the CR through the use of strain gauges [4]. The use of force/torque sensors limits the bandwidth of the pHRI and makes the interaction less intuitive and agile.

It is possible to teach CR tasks through pHRI without using force sensors. To this end, alternative robot kinematic architectures coupled with backdrivable Low-Ratio Transmissions (LRT) can be used. Alternative robot kinematic

architectures can be used to move the CR actuators toward the base in order to minimize the influence of their inertia on the robot dynamics and payload capabilities while allowing larger and stronger actuators with backdrivable transmissions. This concept is already used in industrial palletizing robots [5], haptic devices [6] and backdrivable pHRI robots [7] [8].

LRT are already used in haptic devices for telesurgery [9] [10] [11] [12]. Yet, not all LRT are mechanically backdrivable. For example, a worm gear cannot be driven by its output (through the worm). Table 1 shows a list of backdrivable LRT and indicates their advantages and disadvantages for pHRI.

Table 1 shows that a capstan drive is a good choice of backdrivable LRT because it has higher stiffness than a belt drive and it has a low backlash like gears or chain drives. This is why it is used in haptic devices [10] [13], highly backdrivable collaborative robots [14] [15] [16] and high precision targeting systems [17] [18] [19] [20]. Having low backlash is very important for robotics applications which require the robot's motors to work in both directions at a high frequency [21] [22]. However, Table 1 also shows that capstan drives have lower stiffness than other LRT such as gears and can be subject to slip error [19] [23].

In order to alleviate these drawbacks, this article presents a novel capstan architecture that increases the stiffness of the transmission by using grooves on the transmission's pulleys. The grooves increase the friction coefficient between the cable and the pulleys, which makes the transmission stiffer. This concept has already been used in cable transmissions for elevators as described in [24] and [25]. Moreover, the novel capstan drive allows multiple cable arrangements, which further increases the stiffness of the transmission.

This paper is structured as follows. In Section II and III, the general modelling of a capstan drive and its torsional stiffness are recalled. The theoretical model used here is based on the work of Werkmeister et al. [26]. Part of this

Table 1: Comparison of different backdrivable LRT.

LRT type	Advantages	Disadvantages
Spur and helical gears	High stiffness	Clearance between
	High torque capability	teeth (backlash)
Belt drive	Transmission over a larger distance	Lower stiffness
	No backlash	Slip error
Chain Drive	High stiffness	Clearance between inner links
		Higher transmission inertia
Cable (capstan drive)	Higher stiffness than belt drive	Lower stiffness than chain and gears
	No backlash	Slip error

model is also used in [23]. Section IV explains how grooves etched along the surface of a capstan drive's pulleys can theoretically increase the friction coefficient between the drive's cable and its pulleys thus increasing the overall stiffness of the capstan drive. The use of grooves in capstan drives has already been presented in [18]. However, this paper presents a novel design for the output pulley of a capstan drive which uses grooves arranged as a multiple helix. This novel design enables different multi-cable arrangements of the capstan drive that can theoretically further increase its torsional stiffness. The novel capstan drive architecture as well as different possible cable arrangements are presented in Section V. The advantages and disadvantages of each of the proposed arrangements are discussed. Section VI then proposes a method to properly arrange the capstan drive's pulleys during the drive's assembly so that the cables can follow a smooth and continuous path while passing from one pulley to the other. Finally, concluding remarks are made in Section VIII.

2 Modelling of a capstan drive

Figure 1 presents the different elements of the capstan drive model. In figure 1, r_1 is the radius of the small input pulley while r_2 is the radius of the large output pulley. The transmission ratio is given by $R = \frac{r_2}{r_1}$. The cable passes from the large pulley to the small pulley and back to the large pulley in a lemniscate shaped pattern indicated by the red arrows in figure 1. A preload tension T_p is applied on the cable by pulling on the cable with a mechanism alike a turnbuckle (at point P_1) and by fixing the other end of the cable to the pulley (at point P_2).

When a torque τ_i is applied on the input pulley, one side

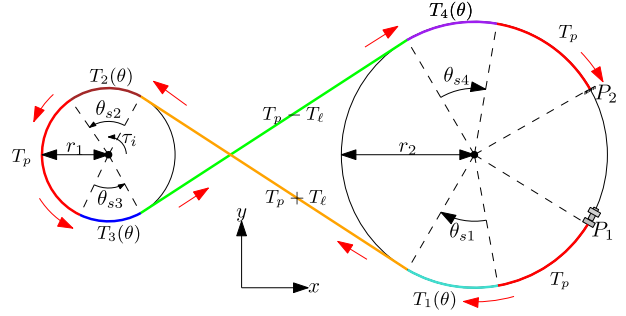


Fig. 1: Modelling of a capstan drive.

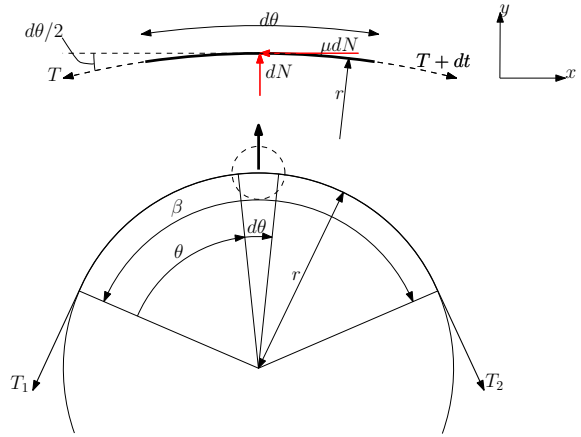


Fig. 2: Small segment of the cable pulley interaction.

of the cable extends while the other part of the cable shortens. The extension is caused by an increase in the tension in the cable by an amount T_ℓ while the contraction of the other part of the cable is caused by a reduction of the tension by an equal amount T_ℓ . The tension on the taught side becomes $T_p + T_\ell$ while the tension on the loose side becomes $T_p - T_\ell$. The torque balance equation about the axis of rotation of the input pulley can be written as

$$\tau_i - (T_p + T_\ell)r_1 + (T_p - T_\ell)r_1 = 0, \quad (1)$$

which yields

$$T_\ell = \frac{\tau_i}{2r_1}. \quad (2)$$

The tension variations in the cable occur in contact regions between the cable and the pulleys called the slip regions. These regions are represented in figure 1 with the angles θ_{s1} to θ_{s4} . Along these slip regions, the cable elongates or shortens due to the applied torque. This local variation in length causes friction between the pulleys and the cable. Figure 2 illustrates this principle.

Figure 2 shows a small segment of a cable lying on the surface of a pulley of radius r . The small cable segment is lying on a small angle segment of the pulley $d\theta$. The static friction coefficient between the pulley and the cable is μ . The

tension on one end of the small cable segment is T while it is $T + dT$ at the other end. The small tension variation is created by an applied torque on the pulley. The normal force between the small cable segment and the pulley is dN . When torque is applied to the pulley, the pulley surface creates a friction force on the cable segment of μdN in the tangential direction of the torque. Calculating the force balance on the cable segment gives

$$\sum F_x = T \cos\left(\frac{d\theta}{2}\right) - (T + dT) \cos\left(\frac{d\theta}{2}\right) + \mu dN = 0, \quad (3)$$

$$\sum F_y = -T \sin\left(\frac{d\theta}{2}\right) - (T + dT) \sin\left(\frac{d\theta}{2}\right) + dN = 0. \quad (4)$$

Since $d\theta$ is a small angle and dT is a small tension variation, the following approximations can be made

$$\sin\left(\frac{d\theta}{2}\right) \approx \frac{d\theta}{2}, \quad \cos\left(\frac{d\theta}{2}\right) \approx 1, \quad dT d\theta \approx 0. \quad (5)$$

Applying these approximations to (3) and (4) gives

$$\frac{dT}{T} = \mu d\theta. \quad (6)$$

In figure 2, when the tension varies from T_1 to T_2 where $T_2 > T_1$, the integration over the angle β of (6) gives

$$\beta = \frac{1}{\mu} \ln\left(\frac{T_2}{T_1}\right). \quad (7)$$

Angle β is referred to as the slip angle of the slip region. Integrating from T_1 to a function $T(\theta)$ over the slip region then gives

$$T(\theta) = T_1 e^{\mu\theta}, \quad 0 < \theta < \beta. \quad (8)$$

The same can be said by integrating from the max tension T_2 to a smaller tension $T(\theta)$ over the slip region β , which gives

$$T(\theta) = T_2 e^{-\mu\theta}, \quad 0 < \theta < \beta. \quad (9)$$

Applying (7), (8) and (9) to the slip regions in figure 1, one

finds

$$T_1(\theta) = T_p e^{\mu\theta}, \quad 0 < \theta < \theta_{s1}, \quad \theta_{s1} = \frac{1}{\mu} \ln\left(\frac{T_p + T_\ell}{T_p}\right), \quad (10)$$

$$T_2(\theta) = (T_p + T_\ell) e^{-\mu\theta}, \quad 0 < \theta < \theta_{s2}, \quad \theta_{s2} = \theta_{s1}, \quad (11)$$

$$T_3(\theta) = T_p e^{-\mu\theta}, \quad 0 < \theta < \theta_{s3}, \quad \theta_{s3} = \frac{1}{\mu} \ln\left(\frac{T_p}{T_p - T_\ell}\right), \quad (12)$$

$$T_4(\theta) = (T_p - T_\ell) e^{\mu\theta}, \quad 0 < \theta < \theta_{s4}, \quad \theta_{s4} = \theta_{s3}. \quad (13)$$

Equations (10) to (13) describe the variation of the tension along the cable. These equations are used in the following section to model the stiffness of a capstan drive.

3 Stiffness model of a capstan drive

Hooke's law gives the relationship between the tensile force in an elastic object and its strain. The strain of an elastic object is also defined as its variation in length over its original length. Expressing this definition of strain in an infinitesimal form and equating it to Hooke's law, one can then write

$$\varepsilon \equiv \frac{d\delta}{dL} = \frac{F}{AE}, \Rightarrow d\delta = \frac{F dL}{AE} \quad (14)$$

where ε is the strain, $d\delta$ is a very small length variation, dL is a very small cable length, F is the tensile force applied on the elastic object, A is the object's cross section area and E is its Young modulus. Equation (14) can be integrated to determine the cable deformation.

The cable deformation δ_i along the slip region θ_{si} is equal to the total deformation along the slip region minus the initial deformation caused by the preload. Using (14) and using the fact that $dL = r d\theta$, the deformations δ_i are obtained as

$$\delta_i = \frac{r}{AE} \left(\int_0^{\theta_{si}} T_i(\theta) d\theta - T_p \int_0^{\theta_{si}} d\theta \right), \quad i = 1, \dots, 4 \quad (15)$$

where $r = r_2$ for θ_{s1} and θ_{s4} and $r = r_1$ for θ_{s2} and θ_{s3} . Applying (15) to the slip angle θ_{s1} gives

$$\delta_1 = \frac{T_p r_2}{AE} \left(\int_0^{\theta_{s1}} e^{\mu\theta} d\theta - \int_0^{\theta_{s1}} d\theta \right), \quad (16)$$

$$= \frac{T_p r_2}{AE} \left(\frac{1}{\mu} (e^{\mu\theta_{s1}} - 1) - \theta_{s1} \right), \quad (17)$$

$$= \frac{r_2}{\mu AE} \left(T_\ell - T_p \ln\left(\frac{T_p + T_\ell}{T_p}\right) \right). \quad (18)$$

Similarly for δ_2 to δ_4 , one obtains

$$\delta_2 = \frac{r_1}{\mu AE} \left(T_\ell - T_p \ln \left(\frac{T_p + T_\ell}{T_p} \right) \right), \quad (19)$$

$$\delta_3 = \frac{r_1}{\mu AE} \left(T_\ell - T_p \ln \left(\frac{T_p}{T_p - T_\ell} \right) \right), \quad (20)$$

$$\delta_4 = \frac{r_2}{\mu AE} \left(T_\ell - T_p \ln \left(\frac{T_p}{T_p - T_\ell} \right) \right). \quad (21)$$

Some cable deformation also occurs in the cable sections which are not in contact with the pulleys. These cable sections are here called the free sections and the deformation along these sections is obtained by integrating (14) which gives

$$\delta_{f1} = \frac{T_p + T_\ell}{AE} \int_0^{L_f} dL = \frac{T_p + T_\ell}{AE} L_f, \quad (22)$$

$$\delta_{f2} = \frac{T_p - T_\ell}{AE} \int_0^{L_f} dL = \frac{T_p - T_\ell}{AE} L_f, \quad (23)$$

where δ_{f1} and δ_{f2} are the deformations on the tight and slack side respectively and L_f is the length of the free parts of the cable which are not in contact with the pulleys.

The compliance of the different cable sections can be defined as the absolute value of the variation in deformation of the cable as a function of the applied load. Mathematically, this means that the compliance of the different cable sections can be obtained by differentiating the deformation expressions in (18) to (23) with respect to T_ℓ . Furthermore, since compliance is the inverse of stiffness, one can easily obtain the stiffness of the different cable sections. For the slip regions, this gives

$$C_{si} = \left| \frac{d\delta_{si}}{dT_\ell} \right|, \quad i = 1, \dots, 4, \quad (24)$$

$$\Rightarrow C_{s1} = \frac{r_2}{AE\mu} \left(\frac{T_\ell}{T_p + T_\ell} \right) = \frac{1}{K_{s1}} \quad (25)$$

$$\Rightarrow C_{s2} = \frac{r_1}{AE\mu} \left(\frac{T_\ell}{T_p + T_\ell} \right) = \frac{1}{K_{s2}} \quad (26)$$

$$\Rightarrow C_{s3} = \frac{r_1}{AE\mu} \left(\frac{T_\ell}{T_p - T_\ell} \right) = \frac{1}{K_{s3}} \quad (27)$$

$$\Rightarrow C_{s4} = \frac{r_2}{AE\mu} \left(\frac{T_\ell}{T_p - T_\ell} \right) = \frac{1}{K_{s4}} \quad (28)$$

For the stiffnesses of the free sections of the cable, one obtains

$$K_{f1} = K_{f2} = \frac{AE}{L_f} \quad (29)$$

The total stiffness of the capstan transmission is obtained by combining the individual stiffnesses of the cable segments along the transmission. The stiffness elements K_{s1}, K_{f1} and

K_{s2} form a serial combination of springs. The same can be said for K_{s3}, K_{f2} and K_{s4} . The two serial springs groups are in parallel to one another meaning that the total stiffness of the transmission can be written as

$$K = K_1 + K_2, \quad (30)$$

where

$$K_1 = \frac{1}{\frac{1}{K_{s1}} + \frac{1}{K_{f1}} + \frac{1}{K_{s2}}}, \quad (31)$$

$$K_2 = \frac{1}{\frac{1}{K_{s3}} + \frac{1}{K_{f2}} + \frac{1}{K_{s4}}}. \quad (32)$$

The total stiffness K represents the linear stiffness of the transmission. Since a capstan drive is a torsional element, a better indicator of its stiffness is the drive's torsional stiffness when one of its pulleys is held rigidly. The torsional stiffness K_t of the capstan drive when the small pulley is held rigidly and a torque τ is applied on the large pulley, causing an angular displacement α , is then given by

$$\tau = K_t \alpha. \quad (33)$$

The relationship between K_t and K is obtained by writing

$$\frac{\tau_D}{r_2} = K \delta \quad (34)$$

$$\alpha = \frac{\delta}{r_2}. \quad (35)$$

Equation (34) gives the relationship between a torque τ applied on the large pulley of radius r_2 and the total linear displacement δ when the small pulley is held tightly. Equation (35) gives the relationship between the total linear displacement of the cable and the angular displacement α of the large pulley of radius r_2 . Using these two equations with (33) yields

$$K_t = K r_2^2. \quad (36)$$

The following section shows how placing the capstan transmission's cable into grooves helps to increase the coefficient of friction between the cable and the pulleys and therefore the transmission's stiffness.

4 Influence of grooves on the capstan drive stiffness

Analyzing the equations for the stiffness of the different cable sections of a capstan drive ((32) to (35)), one can clearly see that all the stiffness terms are proportional to the coefficient of friction. Therefore, Increasing the coefficient of friction between the cable and the pulleys is an effective

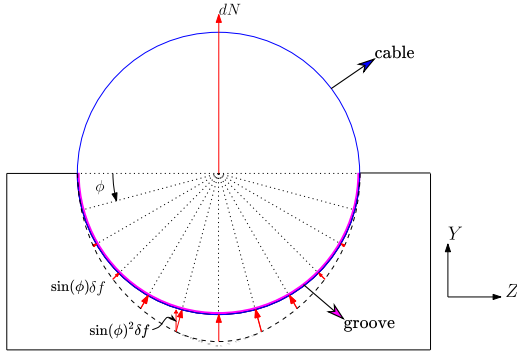


Fig. 3: Distribution of the normal force along the cross-section interface between the cable and the pulleys.

way to increase the overall stiffness of the transmission. Typically, the coefficient of friction is a property that is only dependant on the nature of the materials at the friction interface. However, like for a v-belt drive, by changing the geometry of the interface between two surfaces, it is possible to change the apparent coefficient of friction. Figure 3 illustrates how circular grooves help to increase the coefficient of friction between the cable and the capstan drive pulleys.

The illustrations in figure 3 show the distribution of the normal force occurring between a small section of the cable and a pulley groove. In figure ??, the distribution of the normal force is considered to be uniform along the interface between the cable and the groove. The figure shows the cross section of the interface which is perpendicular to the plane shown in figure 2. The equivalent normal force between the small cable segment and the pulley segment is noted dN and can be mathematically obtained as

$$dN = \int_0^\pi \delta f \sin \phi d\phi = 2\delta f, \quad (37)$$

where ϕ is the variable angle along the interface cross section and δf is a unit force quantity. Applying Coulomb's law of static friction to the cross-section in figure ?? gives

$$dF_f = \int_0^\pi \mu \delta f d\theta = \pi \mu \delta f, \quad (38)$$

where dF_f is the friction force between the cable segment and the cable pulley. Combining (37) and (38) gives

$$dF_f = \mu' dN = \frac{\pi \mu}{2} dN, \quad (39)$$

where μ' is the effective coefficient of friction between the cable and the pulley grooves. Equation (39) shows that, when considering a uniform distribution along the cross section of the cable pulley interface, grooves can help to increase the effective friction coefficient by a factor of $\pi/2$. However, this force distribution along the interface arc is very unlikely considering the fact that local normal force around the middle of the cross-section arc is likely larger than the one at

each extremity of the cross-section arc. Considering this, figure ?? shows how the force could be distributed along the cross-section arc if a general force distribution function $g(\phi)$ is considered. The effective friction coefficient given this consideration is then obtained by

$$dN = \delta f I_1(\phi) = \delta f \int_0^\pi g(\phi) \sin \phi d\phi, \quad (40)$$

$$dF_f = \mu \delta f I_2(\phi) = \mu \delta f \int_0^\pi \mu g(\phi) d\phi. \quad (41)$$

$$dF_f = \mu' dN = \frac{\mu I_2(\phi)}{I_1(\phi)} dN. \quad (42)$$

For any type of positive distribution function $g(\phi)$, the ratio of $\frac{I_2(\phi)}{I_1(\phi)}$ will always be greater than 1. This means that a groove can only increase the effective friction coefficient between the cable and the pulleys of a capstan drive and will therefore make it stiffer.

The following section presents a novel capstan drive architecture that takes advantage of the increased effective friction coefficient of grooved pulleys and uses multiple grooves on its output pulley in order to allow different cable arrangements which further increase the stiffness of the drive.

4.1 Second-Level Heading

The next level of heading is also boldface with upper and lower case letters. The heading is flushed left with the left margin. The spacing to the next heading is two line spaces.

4.1.1 Third-Level Heading.

The third-level of heading follows the style of the second-level heading.

5 Use of SI Units

An ASME paper should use SI units. When preference is given to SI units, the U.S. customary units may be given in parentheses or omitted. When U.S. customary units are given preference, the SI equivalent *shall* be provided in parentheses or in a supplementary table.

6 Footnotes¹

Footnotes are referenced with superscript numerals and are numbered consecutively from 1 to the end of the paper². Footnotes should appear at the bottom of the column in which they are referenced.

7 Mathematics

Equations should be numbered consecutively beginning with (1) to the end of the paper, including any appendices.

¹Examine the input file, asme2ej.tex, to see how a footnote is given in a head.

²Avoid footnotes if at all possible.

Beautiful Figure

Fig. 4: The caption of a single sentence does not have period at the end

The number should be enclosed in parentheses and set flush right in the column on the same line as the equation. An extra line of space should be left above and below a displayed equation or formula. \LaTeX can automatically keep track of equation numbers in the paper and format almost any equation imaginable. An example is shown in Eqn. (43). The number of a referenced equation in the text should be preceded by Eqn. unless the reference starts a sentence in which case Eqn. should be expanded to Equation.

$$f(t) = \int_{0+}^t F(t)dt + \frac{dg(t)}{dt} \quad (43)$$

8 Figures

All figures should be positioned at the top of the page where possible. All figures should be numbered consecutively and centered under the figure as shown in Fig. 4. All text within the figure should be no smaller than 7 pt. There should be a minimum two line spaces between figures and text. The number of a referenced figure or table in the text should be preceded by Fig. or Tab. respectively unless the reference starts a sentence in which case Fig. or Tab. should be expanded to Figure or Table.

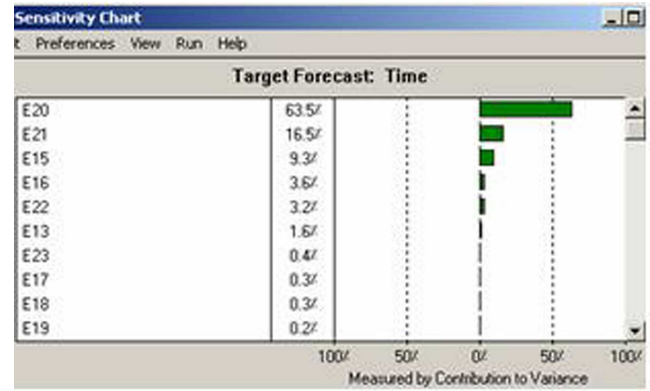
In the following subsections, I have inserted figures that have been provided by authors in order to demonstrate what to avoid. In each case the authors provided figures that are 3.25in wide and 600dpi in the .tif graphics format. The papers containing these figures have been held from production due to their poor quality.

8.1 The 1st Example of Bad Figure

In order to place the figure in this template using MSWord, select Insert Picture from File, and use wrapping that is top and bottom. Make sure the figure is 3.25in wide.

Figure '5 was taken from a recent paper that was held from publication, because the text is fuzzy and unreadable. It was probably obtained by taking a screen shot of the computer output of the authors software. This means the original figure was 72dpi (dots per inch) on a computer screen. There is no way to improve the quality such a low resolution figure.

In order to understand how poor the quality of this figure is, please zoom in slightly, say to 200%. Notice that while the font of the paper is clear at this size, the font in the figures is fuzzy and blurred. It is impossible to make out the small symbol beside the numbers along the abscissa of the graph. Now consider the labels Time and Cost. They are clearly in fonts larger than the text of the article, yet the pixilation



(a) Time



(b) Cost

Fig. 5: Example taken from a paper that was held from production because the image quality is poor. ASME sets figures captions in 8pt, Helvetica Bold.

or rasterization, associated with low resolution is obvious. This figure must be regenerated at higher resolution to ensure quality presentation.

The poor quality of this figure is immediately obvious on the printed page, and reduces the impact of the research contribution of the paper, and in fact detracts from the perceived quality of the journal itself.

8.2 The 2nd Example of Bad Figure

Figure 6 demonstrates a common problem that arises when a figure is scaled down fit a single column width of 3.25in. The original figure had labels that were readable at full size, but become unreadable when scaled to half size. This figure also suffers from poor resolution as is seen in the jagged lines the ovals that form the chain.

This problem can be addressed by increasing the size of the figure to a double column width of 6.5in, so the text is readable. But this will not improve the line pixilation, and a large low resolution figure is less desirable than a small one. This also significantly expands the length of the paper, and

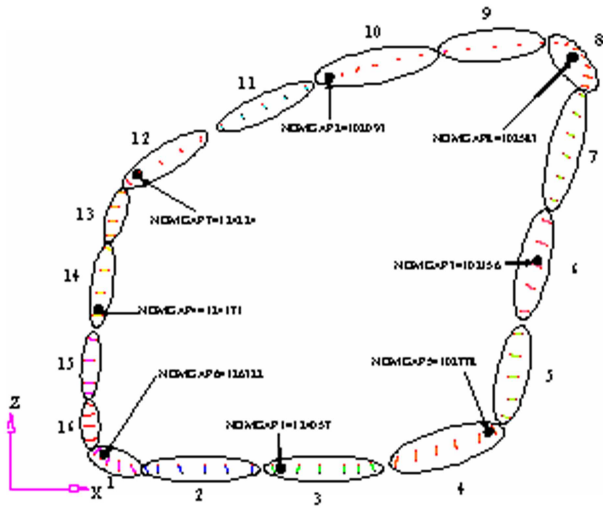


Fig. 6: While this figures is easily readable at a double column width of 6.5in, when it is shrunk to 3.25in column width the text is unreadable. This paper was held from production.

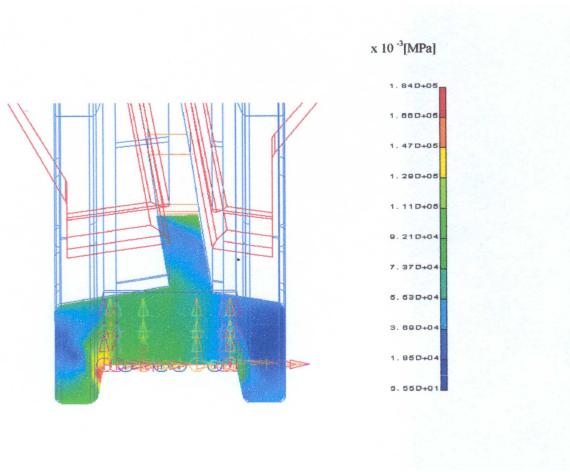


Fig. 7: Another example of a figure with unreadable text. Even when the paper was expanded to double column width the text as shown in Fig. 8 was of such low quality that the paper was held from production.

may cause it to exceed the JMD nine page limit. Additional pages require page charges of \$200 per page. It is best to regenerate the figure at the resolution that ensures a quality presentation.

8.3 The 3rd Example of Bad Figure

An author provided the high resolution image in Fig. 7 that was sized to a single column width of 3.25in. Upon seeing the poor quality of the text, the publisher scaled the image to double column width as shown in Fig. 8 at which point it took half of a page. The publisher went on to do this for all eight figures generating four pages of figures that

Table 2: Figure and table captions do not end with a period

Example	Time	Cost
1	12.5	\$1,000
2	24	\$2,000

the author did not expect. ASME stopped production of the paper even with the larger figures due to the pixilation of the font.

Clearly the text in this figure is unreadable, and it is doubtful that the author can print the output in a way that it is readable. This is a problem that the author must solve, not the publisher.

As you might expect, I have many more examples, but in the end the author is the best judge of what is needed in each figure. ASME simply requires that the image meet a minimum standard for font and line quality, specifically the font should be the appropriate size and not be blurred or pixilated, and that lines should be the appropriate weight and have minimal, preferably no, pixilation or rasterization.

9 Tables

All tables should be numbered consecutively and centered above the table as shown in Table 2. The body of the table should be no smaller than 7 pt. There should be a minimum two line spaces between tables and text.

10 Citing References

The ASME reference format is defined in the authors kit provided by the ASME. The format is:

Text Citation. Within the text, references should be cited in numerical order according to their order of appearance. The numbered reference citation should be enclosed in brackets.

The references must appear in the paper in the order that they were cited. In addition, multiple citations (3 or more in the same brackets) must appear as a “ [1-3]”. A complete definition of the ASME reference format can be found in the ASME manual [?].

The bibliography style required by the ASME is unsorted with entries appearing in the order in which the citations appear. If that were the only specification, the standard `BIBTeX unsrt` bibliography style could be used. Unfortunately, the bibliography style required by the ASME has additional requirements (last name followed by first name, periodical volume in boldface, periodical number inside parentheses, etc.) that are not part of the `unsrt` style. Therefore, to get ASME bibliography formatting, you must use the `asmems4.bst` bibliography style file with `BIBTeX`. This file is not part of the standard `BibTeX` distribution so you’ll

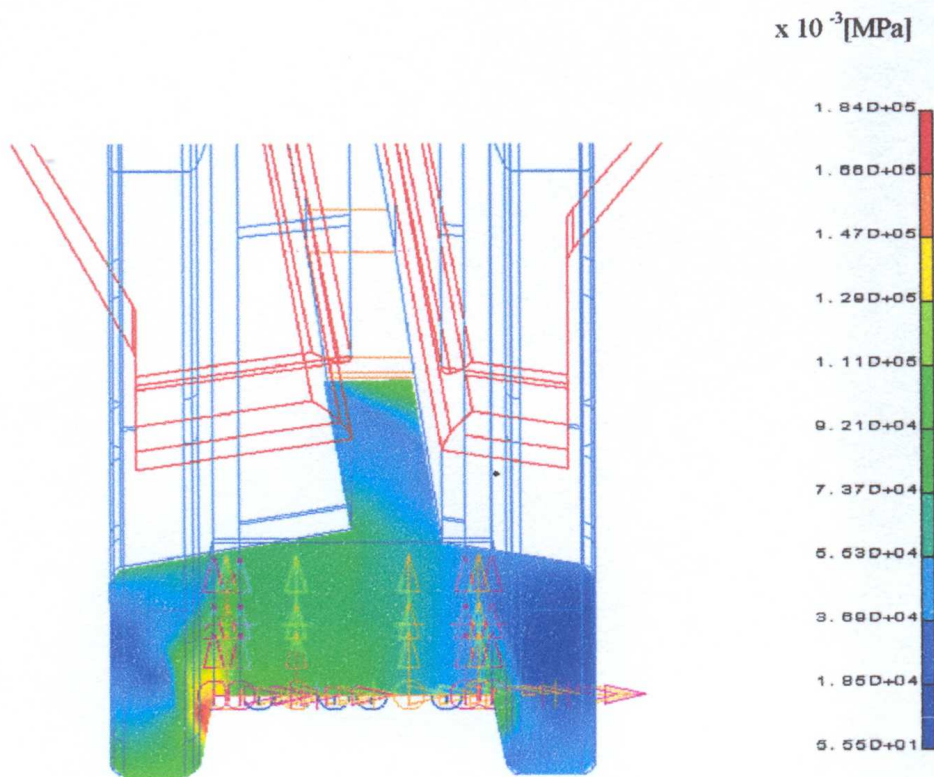


Fig. 8: A figure expanded to double column width the text from Figure 7

need to place the file someplace where LaTeX can find it (one possibility is in the same location as the file being typeset).

With \LaTeX /BIB \TeX , \LaTeX uses the citation format set by the class file and writes the citation information into the .aux file associated with the \LaTeX source. BIB \TeX reads the .aux file and matches the citations to the entries in the bibliographic data base file specified in the \LaTeX source file by the `\bibliography` command. BIB \TeX then writes the bibliography in accordance with the rules in the bibliography .bst style file to a .bbl file which \LaTeX merges with the source text. A good description of the use of BIB \TeX can be found in [?, ?] (see how two references are handled?). The following is an example of how three or more references [?, ?, ?] show up using the `asme4.bst` bibliography style file in conjunction with the `asme2ej.cls` class file. Here are some more [?, ?, ?, ?, ?, ?, ?, ?, ?] which can be used to describe almost any sort of reference.

11 Conclusions

The only way to ensure that your figures are presented in the ASME Journal of Mechanical Design in the way you feel is appropriate and meets the requirement for quality pre-

sensation is for you to prepare a double column version of the paper in a form similar to that used by the Journal.

This gives you the opportunity to ensure that the figures are sized appropriately, in particular that the labels are readable and match the size of the text in the journal, and that the line weights and resolutions have no pixilation or rasterization. Poor quality figures are immediately obvious on the printed page, and this detracts from the perceived quality of the journal.

I am pleased to provide advice on how to improve any figure, but this effort must start with a two-column version of the manuscript. Thank you in advance for your patience with this effort, it will ensure quality presentation of your research contributions.

12 Discussions

This template is not yet ASME journal paper format compliant at this point. More specifically, the following features are not ASME format compliant.

1. The format for the title, author, and abstract in the cover page.
2. The font for title should be 24 pt Helvetica bold.

If you can help to fix these problems, please send us an updated template. If you know there is any other non-compliant item, please let us know. We will add it to the above list. With your help, we shall make this template compliant to the ASME journal paper format.

Acknowledgements

This work was supported by the Natural Sciences and Engineering Research Council of Canada (NSERC) and by the Canada Research Chair Program.

References

- [1] Roveda, L., Pedrocchi, N., Beschi, M., and Tosatti, L. M., 2018. “High-accuracy robotized industrial assembly task control schema with force overshoots avoidance”. *Control Engineering Practice*, **71**, pp. 142–153.
- [2] Meißner, D.-W. I. J., Schmatz, M. S. F., Beuß, D.-I. F., Sender, D.-W. I. J., Flügge, I. W., and Gorr, D.-K. F. E., 2018. “Smart human-robot-collaboration in mechanical joining processes”. *Procedia Manufacturing*, **24**, pp. 264–270.
- [3] Raessa, M., Sánchez, D., Wan, W., Petit, D., and Harada, K., 2019. “Teaching a robot to use electric tools with regrasp planning”. *CAAI Transactions on Intelligence Technology*, **4**(1), pp. 54–63.
- [4] Loughlin, C., Albu-Schäffer, A., Haddadin, S., Ott, C., Stemmer, A., Wimböck, T., and Hirzinger, G., 2007. “The dlr lightweight robot: design and control concepts for robots in human environments”. *Industrial Robot: an international journal*.
- [5] Xiaoqing, G., and Jidong, W., 2011. “Mechanical design and kinematic analysis of a new kind of palletizing robot”. In 2011 Second International Conference on Mechanic Automation and Control Engineering, IEEE, pp. 404–408.
- [6] 3d systems, 2020. Phantom premium. On the WWW, August. URL <https://www.3dsystems.com/haptics-devices/3d-systems-phantom-premium>.
- [7] Wen, K., Harton, D., Laliberté, T., and Gosselin, C., 2019. “Kinematically redundant (6+ 3)-dof hybrid parallel robot with large orientational workspace and remotely operated gripper”. In 2019 International Conference on Robotics and Automation (ICRA), IEEE, pp. 1672–1678.
- [8] Wen, K., Nguyen, T. S., Harton, D., Laliberté, T., and Gosselin, C., 2020. “A backdrivable kinematically redundant (6+3)-degree-of-freedom hybrid parallel robot for intuitive sensorless physical human-robot interaction”. *IEEE Transactions on Robotics*, pp. 1–17.
- [9] Gosselin, F., Ferlay, F., Bouchigny, S., Mégard, C., and Taha, F., 2011. “Specification and design of a new haptic interface for maxillo facial surgery”. In 2011 IEEE International Conference on Robotics and Automation, IEEE, pp. 737–744.
- [10] Perret, J., and Vercruysse, P., 2014. “Advantages of mechanical backdrivability for medical applications of force control”. In Workshop on Computer/Robot Assisted Surgery (CRAS).
- [11] Baumann, R., and Clavel, R., 1998. “Haptic interface for virtual reality based minimally invasive surgery simulation”. In Proceedings. 1998 IEEE International Conference on Robotics and Automation (Cat. No. 98CH36146), Vol. 1, IEEE, pp. 381–386.
- [12] Carignan, C. R., and Cleary, K. R., 2000. “Closed-loop force control for haptic simulation of virtual environments”.
- [13] Baser, O., and Konukseven, E. I., 2013. “Kinematic model calibration of a 7-dof capstan-driven haptic device for pose and force control accuracy improvement”. *Proceedings of the Institution of Mechanical Engineers, Part C: Journal of Mechanical Engineering Science*, **227**(6), pp. 1328–1340.
- [14] Townsend, W. T., 1988. “The effect of transmission design on force-controlled manipulator performance”. PhD thesis.
- [15] Rooks, B., 2006. “The harmonious robot”. *Industrial Robot: An International Journal*, **33**(2), pp. 125–130.
- [16] Phan, S., Lioulemes, A., Lutterodt, C., Makedon, F., and Metsis, V., 2014. “Guided physical therapy through the use of the barrett wam robotic arm”. In 2014 IEEE International Symposium on Haptic, Audio and Visual Environments and Games (HAVE) Proceedings, IEEE, pp. 24–28.
- [17] Lu, Y., Liao, H., Hei, M., Liu, H., and Fan, D., 2015. “Development of a differential cable drive mechanism for acquiring tracking and pointing application”. *Proceedings of the Institution of Mechanical Engineers, Part C: Journal of Mechanical Engineering Science*, **229**(17), pp. 3191–3200.
- [18] Lu, Y., and Fan, D., 2012. “Non-intervene cable wrapping method for precise cable drive”. In 2012 international conference on optoelectronics and microelectronics, IEEE, pp. 378–383.
- [19] Lu, Y., and Fan, D., 2013. “Transmission backlash of precise cable drive system”. *Proceedings of the Institution of Mechanical Engineers, Part C: Journal of Mechanical Engineering Science*, **227**(10), pp. 2256–2267.
- [20] Xie, X., Qi, C., Zhang, L., and Fan, D., 2019. “Analytical and experimental research on transmission backlash in precise cable drive for an electro-optical targeting system”. *Advances in Mechanical Engineering*, **11**(7), p. 1687814019866059.
- [21] Brooks, T. L., 1990. “Telerobotic response requirements”. In 1990 IEEE International Conference on Systems, Man, and Cybernetics Conference Proceedings, IEEE, pp. 113–120.
- [22] Gealy, D. V., McKinley, S., Yi, B., Wu, P., Downey, P. R., Balke, G., Zhao, A., Guo, M., Thomasson, R., Sinclair, A., et al., 2019. “Quasi-direct drive for low-cost compliant robotic manipulation”. In 2019 International Conference on Robotics and Automation (ICRA), IEEE, pp. 437–443.

- [23] Baser, O., and Konukseven, E. I., 2010. “Theoretical and experimental determination of capstan drive slip error”. *Mechanism and Machine Theory*, **45**(6), pp. 815–827.
- [24] Gibson, G. W. “Fred hymans and the theory of rope traction, part one”. *Elevator World*.
- [25] Hymans, F., and Hellborn, A., 2013. *Der neuzeitliche Aufzug mit Treibscheibenantrieb: Charakterisierung, Theorie, Normung*. Springer-Verlag.
- [26] Werkmeister, J., and Slocum, A., 2007. “Theoretical and experimental determination of capstan drive stiffness”. *precision Engineering*, **31**(1), pp. 55–67.

Appendix A: Head of First Appendix

Avoid Appendices if possible.

Appendix B: Head of Second Appendix

Subsection head in appendix

The equation counter is not reset in an appendix and the numbers will follow one continual sequence from the beginning of the article to the very end as shown in the following example.

$$a = b + c. \tag{44}$$